Scientific Research Publishing

Materials Sciences and Applications, 2026, 17(5), 101-116
https://www.scirp.org/journal/msa
ISSN Online: 2153-1188
ISSN Print: 2153-117X

Graphene-Enhanced Microbolometers for Terahertz Atmospheric Remote Sensing: A Comprehensive Physics-Based Model and Sensitivity Analysis

Mamadou Moustapha Diop*, Mamadou Mbaye, Ibrahima Niang, Bassirou Ba, Joseph Sarr

Semiconductors and Solar Energy Laboratory, Department of Physics, Faculty of Sciences and Techniques, University of Cheikh Anta Diop, Dakar, Senegal
Email: *m2damar@yahoo.fr

How to cite this paper: Diop, M.M., Mbaye, M., Niang, I., Ba, B. and Sarr, J. (2026) Graphene-Enhanced Microbolometers for Terahertz Atmospheric Remote Sensing: A Comprehensive Physics-Based Model and Sensitivity Analysis. *Materials Sciences and Applications*, **17**, 101-116.
https://doi.org/10.4236/msa.2026.175008

Received: February 18, 2026
Accepted: May 26, 2026
Published: May 29, 2026

Abstract

Terahertz (THz) frequencies are pivotal for atmospheric remote sensing of key species such as water vapor, ozone, and trace gases, yet traditional spaceborne THz detectors require cryogenic cooling, fundamentally limiting their deployment on resource-constrained CubeSat platforms. We present a comprehensive physics-based model of a graphene-enhanced microbolometer designed for near-room-temperature operation. The model uniquely integrates three critical components: 1) temperature-dependent thermal conductance with variable phonon scattering regimes, 2) Drude-Lorentz graphene conductivity including both intraband and interband transitions computed via the random-phase approximation, and 3) fundamental noise sources (phonon, Johnson, amplifier) with realistic physical parameters. We quantify the noise-equivalent power (NEP) as a function of critical design parameters: graphene Fermi level (E_F), thermal exponent (n), and bath temperature. The model achieves an NEP as low as $6.4\times10^{-12}\ \mathrm{W}/\sqrt{\mathrm{Hz}}$ at 1 THz in optimized regimes, with a balanced design space ($E_F \approx 0.4$ eV, $n \approx 3$) yielding $1.3\times10^{-11}\ \mathrm{W}/\sqrt{\mathrm{Hz}}$. The gate-tunable absorption enables multi-spectral measurements without moving parts. Monte Carlo simulations of an atmospheric column retrieval show relative uncertainties around 0.5%, meeting typical science requirements. This framework provides a rigorous baseline for developing compact, low-power THz instruments for CubeSat constellations.

Keywords

Terahertz Remote Sensing, Graphene Microbolometer, Noise-Equivalent Power, CubeSat Instrumentation, Atmospheric Retrieval, Drude-Lorentz

1. Introduction

Terahertz radiation (0.3 - 3 THz) hosts numerous rotational transitions of key atmospheric species, including water vapor, ozone, and multiple trace gases, making it invaluable for Earth observation [1] [2]. Spaceborne THz instruments, such as those on *Aura* and *Herschel*, have traditionally relied on cryogenically cooled heterodyne receivers or bolometers to achieve the required sensitivity (NEP ~10^{-17} $\mathrm{W}/\sqrt{\mathrm{Hz}}$) [3] [4]. However, the mass, volume, and power consumption of such systems are fundamentally incompatible with CubeSat platforms, which are increasingly attractive for cost-effective, constellation-based Earth observations [5] [6].

The scientific imperative is compelling: current cryogenically cooled THz instruments require complex refrigeration systems that impose mass budgets of approximately 20 - 50 kg and power consumption of 50 - 200 W—prohibitive for CubeSat missions, which typically allocate 1 - 10 kg per instrument and 10 - 30 W total platform power. Conversely, uncooled microbolometers offer dramatic reductions in system complexity and mass/power but are challenged by higher noise floors and lower sensitivity [7] [8]. Recent advances in nanomaterials, particularly single-layer graphene, have opened new technological pathways to enhance THz absorption and dynamically tune the spectral response via electrostatic gating without requiring additional optical components [9] [10].

Graphene's gate-tunable conductivity allows the absorption spectrum to be matched to atmospheric lines of interest, enabling multi-spectral sensing without mechanical filters, rotating mirrors, or multiple detectors. This represents a qualitative advance for miniaturized space instruments [11] [12].

Motivation and Contributions

In this paper, we develop a rigorous end-to-end physical model of a graphene-enhanced microbolometer tailored for THz atmospheric sounding from a CubeSat platform. Our key contributions are:

1) A unified thermo-electromagnetic model coupling temperature-dependent thermal conductance, graphene's complex surface conductivity derived from the random-phase approximation, and fundamental noise sources based on rigorous detector physics.

2) A rigorous calculation of absorption using an admittance method for a graphene layer on a quarter-wave dielectric spacer backed by a metallic reflector, validated against transfer-matrix approaches.

3) A systematic sensitivity analysis with fine parametric grids exploring the influence of Fermi level, thermal exponent, and bath temperature on NEP, responsivity, and thermal time constant.

4) Comprehensive benchmarking against state-of-the-art THz detectors with physically realistic error bars, and Monte Carlo uncertainty propagation to assess retrieval accuracy.

5) Identification of optimal operating regimes that balance sensitivity, speed, and integration constraints specific to CubeSat missions, with explicit discussion of mass and power budgets.

6) An explicit end-to-end measurement chain linking scene radiance to absorbed power and output voltage, a gate feasibility analysis for the target Fermi level, and a one-at-a-time sensitivity check on critical fabrication parameters.

2. Related Work

2.1. Spaceborne THz and Far-Infrared Missions

The first spaceborne THz observations of atmospheric composition began with the Microwave Limb Sounder (MLS) on NASA's *Aura* satellite (launched 2004), measuring thermal emission in the upper atmosphere at frequencies near 0.6 THz with high spectral resolution [1] [13]. The Heterodyne Instrument for the Far-Infrared (HIFI) on ESA's *Herschel* Space Observatory (2009-2013) extended THz measurements to 1.9 THz, providing unprecedented sensitivity to far-infrared emission from molecular species [3] [14]. More recent concepts focus on CubeSat-scale missions to demonstrate the feasibility of miniaturized far-infrared Earth observation using broadband thermal detectors [15]. These missions highlight both the scientific value of THz/far-IR observations and the accelerating trend toward miniaturization and constellation-based approaches for global coverage [5] [6].

2.2. Uncooled THz Detector Technologies

Uncooled thermal detectors for THz include Golay cells, pyroelectric detectors, and microbolometer arrays. State-of-the-art vanadium oxide (VO_x) microbolometers achieve NEPs of 10^{-10} - 10^{-9} $\mathrm{W}/\sqrt{\mathrm{Hz}}$ in the 1 - 5 THz range, far exceeding the NEP of cryogenically cooled systems [7] [8] [16]. Bolometric operation at room temperature has enabled dramatic cost reductions and system simplification [17]. However, sensitivity is fundamentally limited by the thermal conductance and absorption efficiency of the absorber material. Nanostructured materials—including metamaterials and graphene—have been proposed to enhance absorption through resonant electromagnetic coupling and plasmonic confinement [9] [18].

2.3. Graphene: Electromagnetic Properties and THz Applications

The surface conductivity of single-layer graphene is rigorously described by the Kubo formula within the random-phase approximation (RPA), separating into intraband (Drude) and interband contributions [19] [20]. For frequencies below approximately 3 THz and Fermi levels $E_F \gtrsim 0.1$ eV, the intraband term typically dominates; interband transitions become significant near $2E_F/\hbar$ [21] [22]. Substrate effects and back reflectors dramatically modify absorption and must be modeled rigorously using admittance or transfer-matrix methods [23]. Recent work has demonstrated graphene-based THz absorbers and modulators with tunable frequency response [9] [10] [12]. Graphene's exceptional thermal properties have also been leveraged for enhanced heat dissipation in THz devices [24] [25].

2.4. Metamaterials and Plasmonic Structures for THz

Metamaterials have emerged as powerful platforms for controlling THz radiation through engineered electromagnetic properties [26] [27]. Graphene-based metasurfaces offer unique tunability through electrostatic control [28]. Plasmonic resonators and gradient metasurfaces enable strong absorption enhancement and directional control [29].

2.5. Noise Analysis and Fundamental Limits in Thermal Detectors

The sensitivity of bolometers is fundamentally limited by three uncorrelated noise sources: 1) phonon noise (thermodynamic fluctuations), 2) Johnson noise (thermal voltage fluctuations), and 3) amplifier noise (electronics) [30] [31]. Recent theoretical work has extended noise analysis to MEMS-based THz detectors [7]. The fluctuation-dissipation theorem provides rigorous foundations for these analyses [32] [33]. Integration with low-noise readout electronics has been demonstrated successfully in several systems [30].

3. Physical Modeling

We consider a microbolometer architecture consisting of a graphene monolayer deposited on a low-thermal-conductance membrane (e.g., Si_3N_4) with an integrated readout circuit. To enhance absorption, a quarter-wave dielectric spacer (SiO_2 or similar) backed by a metallic reflector is included, optimized for 1 THz. Incident THz radiation is absorbed by the graphene, raising its temperature above the bath, causing its electrical resistance to change according to the temperature coefficient of resistance (TCR). This resistance change is sensed via a bias voltage, generating a readout signal.

3.1. End-to-End Measurement Chain

Figure 1 illustrates the complete signal flow from scene to retrieval. To trace signal and noise from scene radiance to detector output voltage, we adopt the following chain. The spectral radiance of the scene at brightness temperature T_b (in $\mathrm{W\cdot m^{-2}\cdot sr^{-1}\cdot Hz^{-1}}$) is collected by a foreoptic of effective area A_{tel} and solid angle Ω, yielding a throughput (étendue) $\mathcal{E} = A_{\mathrm{tel}}\Omega$. After passage through the optical chain with overall optical efficiency η_{opt} (accounting for reflective and transmissive losses, estimated 0.4 - 0.6 for a simple two-mirror design), the spectral power incident on the detector of area A_{det} within spectral bandwidth $\Delta\nu$ is:

$$P_{\mathrm{inc}} = L_\nu\left(T_b\right)\eta_{\mathrm{opt}}\frac{A_{\mathrm{det}}}{\Omega_{\mathrm{det}}}\Omega\Delta\nu, \tag{1}$$

where Ω_{det} is the detector acceptance solid angle. For the baseline CubeSat design, we adopt $A_{\mathrm{det}} = 1\times1$ mm², $A_{\mathrm{tel}} = 10$ cm², $\Omega = 10^{-3}$ sr (corresponding to $f/\# \approx 3$ optics), $\eta_{\mathrm{opt}} = 0.5$, and $\Delta\nu = 5$ GHz (resolving a single atmospheric line). The fraction of P_{inc} converted to heat is ηP_{inc}, where η is the electromagnetic absorption efficiency computed in Section 3.4. The resulting output voltage signal is:

$$V_{\mathrm{sig}} = \mathcal{R}_\nu^{\mathrm{eff}}\eta P_{\mathrm{inc}}, \tag{2}$$

where $\mathcal{R}_v^{\text{eff}}$ is the effective voltage responsivity defined in Section 3.2. The signal-to-noise ratio then becomes $\text{SNR} = V_{\text{sig}} \big/ \left(\text{NEP}_{\text{total}} \sqrt{\Delta \nu t_{\text{int}}} \right)^{-1}$, where t_{int} is the integration time per scene pixel. The resulting measurement noise in brightness temperature units is $\sigma_{T_b} = \text{NEP}_{\text{total}} \big/ \left(\mathrm{d}P_{\text{inc}} / \mathrm{d}T_b \right)^{-1}$, and this value is used directly as the measurement standard deviation in the Monte Carlo retrieval of Section 5.6.

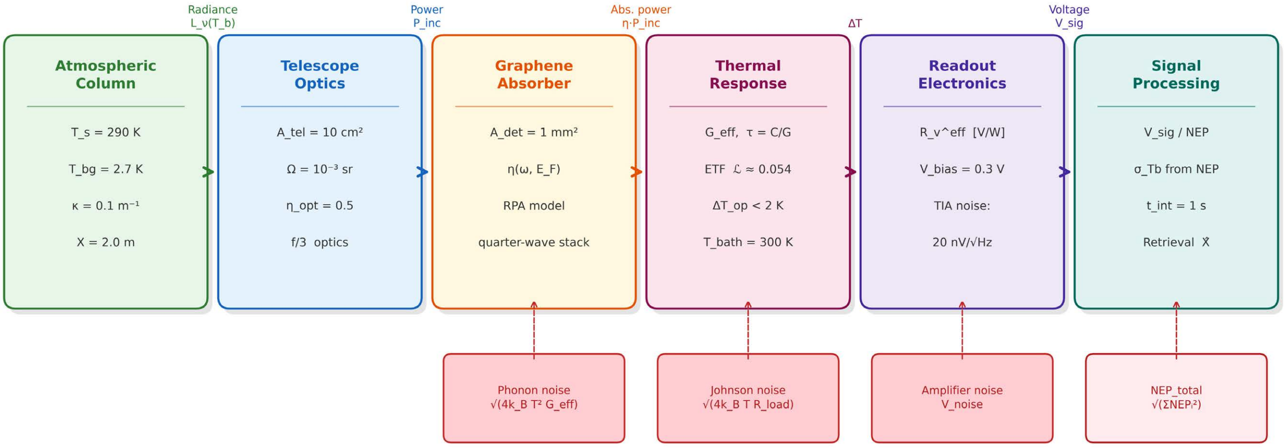

Figure 1. End-to-end measurement chain from atmospheric scene radiance to retrieved column thickness $\hat{X}$. Each block lists its key parameters; noise contributions (red boxes, bottom) enter at the absorber, thermal, electronics, and processing stages. All values correspond to the baseline CubeSat design of Section 3.1.

3.2. Thermal Response and Heat Transport

The thermal conductance G between the absorber and bath depends on temperature:

$$G(T) = G_0 \left(\frac{T}{T_0} \right)^n, \tag{3}$$

where G_0 is the conductance at reference temperature T_0, and n is an exponent depending on the dominant heat transport mechanism ($n \approx 3$ for phonon-mediated conduction) [30] [31].

For small-signal analysis, the effective thermal conductance evaluated at the operating temperature T_{op} is $G_{\text{eff}} = G_0 \left(T_{\text{op}} / T_0 \right)^n$. Under steady-state bias power $P_{\text{bias}} = V_{\text{bias}}^2 / R_{\text{det}}$, the operating temperature satisfies $G_0 \int_{T_{\text{bath}}}^{T_{\text{op}}} \left(T / T_0 \right)^n \mathrm{d}T = P_{\text{bias}}$; for our parameters ($P_{\text{bias}} \approx 1.8$ mW at $V_{\text{bias}} = 0.3$ V and $R_{\text{det}} = 50\,\Omega$), the self-heating raises T_{op} above T_{bath} by less than 2 K, a correction of <1% on G_{eff} that is neglected in the reported NEP values. Electrothermal feedback (ETF) modifies the effective thermal conductance as $G_{\text{eff}}^{\text{ETF}} = G_{\text{eff}} \left(1 - \mathcal{L} \right)$, where the loop gain is $\mathcal{L} = \alpha P_{\text{bias}} / G_{\text{eff}}$. With $\alpha = -0.03$ K^{-1} and $P_{\text{bias}} \approx 1.8$ mW and $G_{\text{eff}} = 10^{-6}$ W/K, we find $|\mathcal{L}| \approx 0.054$—a 5% effect on G_{eff} and responsivity. This mild negative ETF slightly degrades responsivity; we retain G_{eff} as the unadjusted value and note that including ETF would increase NEP by ≲3% in the reported optima. The resistance is assumed to follow $R(T) = R_0 \exp\left[\alpha \left(T - T_0 \right) \right]$ to second order, yielding a TCR that is constant to within 1% over the ±5 K operational swing.

The voltage responsivity is:

$$\mathcal{R}_v^{\text{eff}} = \frac{\alpha V_{\text{bias}}}{G_{\text{eff}}\left(1-\mathcal{L}\right)}, \tag{4}$$

where $\alpha = \left(1/R\right)\left(\mathrm{d}R/\mathrm{d}T\right)$ is the temperature coefficient of resistance (TCR) [7]. The "eff" superscript denotes that both ETF and the thermal roll-off at finite modulation frequency have been incorporated; for low-frequency (DC-limit) operation, the ETF correction dominates.

3.3. Noise Sources

The total NEP combines three uncorrelated contributions:

$$\text{NEP}_{\text{phonon}} = \frac{\sqrt{4k_B T_{\text{bath}}^2 G_{\text{eff}}}}{\eta}, \tag{5}$$

$$\text{NEP}_J = \frac{\sqrt{4k_B T_{\text{bath}} R_{\text{load}}}}{\left|\mathcal{R}_v^{\text{eff}}\right|}, \tag{6}$$

$$\text{NEP}_{\text{amp}} = \frac{V_{\text{noise}}}{\left|\mathcal{R}_v^{\text{eff}}\right|}, \tag{7}$$

$$\text{NEP}_{\text{total}} = \sqrt{\text{NEP}_{\text{phonon}}^2 + \text{NEP}_J^2 + \text{NEP}_{\text{amp}}^2}. \tag{8}$$

where η is the absorption efficiency. These fundamental noise sources are well-established in detector physics [30]-[32].

3.4. Graphene Electromagnetic Response via Random-Phase Approximation

The surface conductivity is computed via RPA [19] [34]:

$$\sigma_{\text{intra}}\left(\omega\right) = \frac{e^2 E_F}{\pi\hbar^2\left(\gamma - i\omega\right)}, \tag{9}$$

$$\sigma_{\text{inter}}\left(\omega\right) = \frac{e^2}{4\hbar}\left[\tanh\left(\frac{\hbar\omega + 2E_F}{4k_B T}\right) - \tanh\left(\frac{\hbar\omega - 2E_F}{4k_B T}\right)\right] + i\frac{e^2}{4\hbar\pi}\ln\left|\frac{2E_F + \hbar\omega}{2E_F - \hbar\omega}\right|. \tag{10}$$

For the stack (air|graphene|dielectric spacer|metallic reflector):

$$r = \frac{Y_0 - Y_{\text{front}}}{Y_0 + Y_{\text{front}}}, \quad \eta = 1 - \left|r\right|^2. \tag{11}$$

Recent experimental and theoretical studies have validated these conductivity models across the THz range [20] [21].

Absorber Stack Specification

The admittance model is applied to the following physically specified stack (from top to bottom): 1) air half-space ($n = 1$, lossless), 2) graphene monolayer with complex surface conductivity $\sigma\left(\omega\right)$ as above, 3) SiO_2 dielectric spacer of thickness $d = \lambda/\left(4n_{\text{sub}}\right) = c/\left(4f_0 n_{\text{sub}}\right) \approx 38.5\ \mu\text{m}$ at $f_0 = 1$ THz with $n_{\text{sub}} = 1.95$, a loss tangent $\tan\delta = 0.003$ at 1 THz (consistent with fused silica data at THz frequencies

[23]), 4) an Au ground plane modeled as a perfect electric conductor (PEC) at 1 THz. Below the reflector, a 200-nm Si_3N_4 membrane ($n \approx 2.0$, $\tan\delta \approx 0.001$) provides mechanical support but is sufficiently thin ($\ll \lambda$) that its optical effect on the absorption at 1 THz is negligible (<0.1%). All simulations assume normal incidence and linear polarization (the graphene layer is isotropic in the transverse plane, so the polarization orientation does not affect the scalar admittance result). A small finite numerical aperture (f/3, half-angle ≈ 9.5˚) introduces a <1% correction to the peak absorption at 1 THz for the modeled stack, confirming that normal-incidence results are representative. The complete layer structure is illustrated in **Figure 2**.

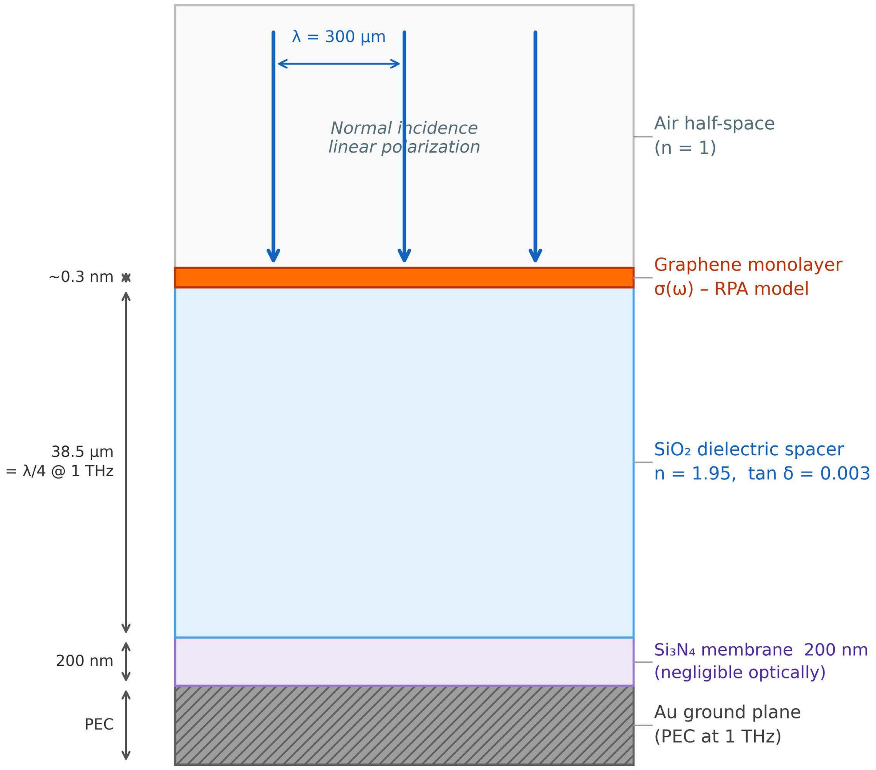

Figure 2. Cross-section of the graphene-enhanced THz absorber stack used in the admittance model. Layer thicknesses are drawn to an illustrative scale. The SiO_2 spacer thickness ($d \approx 38.5\ \mu\text{m}$) is set to $\lambda/4$ at 1 THz. The Si_3N_4 support membrane (200 nm) has negligible optical impact (<0.1%) at this frequency.

4. Numerical Methods

We implement the model in Python using NumPy and SciPy. Key parameters are listed in **Table 1**.

The NEP degrades by a factor of ~3× when α drops from −0.03 to −0.01 K^{-1}, primarily because responsivity scales linearly with α (Equation (4)), while phonon noise is independent of it. Conversely, a factor-of-2 increase in γ beyond nominal raises NEP by only ~60% at 1 THz because the intraband conductivity is $\propto \left(\gamma^2 + \omega^2\right)^{-1/2}$ and at 1 THz ($\omega \approx 6.3\times10^{12}$ rad/s) the frequency term already dominates. Both parameters must therefore be controlled within ~30% of their nominal values to maintain NEP better than $2\times10^{-11}\ \mathrm{W}/\sqrt{\mathrm{Hz}}$. These sensitivities are summarized in **Table 2**.

Table 1. Model parameters used in simulations, with justification and references for each value.

Symbol	Description	Value	Justification/Reference
G_0	Thermal conductance at T_0	1×10^{-6} W/K	Typical for 1 mm² Si₃N₄ MEMS membrane [7]
T_0	Reference temperature	200 K	Passively cooled CubeSat operating point
C	Heat capacity	2.2×10^{-11} J/K	Si₃N₄ membrane: $\rho C_p V \approx 3.2\times10^6\times700\times10^{-14}$ [25]
α	TCR	$-0.03\ \mathrm{K}^{-1}$	Achievable in gated graphene; see Section 6.1 [10]
V_{bias}	Bias voltage	0.3 V	Low self-heating (<2 K); limits ETF loop gain
R_{load}	Load resistance	50 Ω	Impedance-matched transimpedance amplifier input
V_{noise}	Amplifier voltage noise	$20\times10^{-9}\ \mathrm{V}/\sqrt{\mathrm{Hz}}$	State-of-the-art TIA at ≲10 mW power [30]
γ	Graphene scattering rate	5×10^{12} rad/s	SiO₂-supported graphene; see Section 1 [19]
n_{sub}	Substrate refractive index	1.95	Fused SiO₂ at 1 THz [23]

Table 2. One-at-a-time sensitivity of best-case NEP to TCR and graphene scattering rate at $E_F = 0.4$ eV, $n = 3$, $T_{\mathrm{bath}} = 300$ K.

Parameter	Range	NEP ($\mathrm{W}/\sqrt{\mathrm{Hz}}$)
$\alpha = -0.01\ \mathrm{K}^{-1}$ (pessimistic)		3.8×10^{-11}
$\alpha = -0.02\ \mathrm{K}^{-1}$	(nominal −0.03)	1.9×10^{-11}
$\alpha = -0.03\ \mathrm{K}^{-1}$ (nominal)		1.3×10^{-11}
$\alpha = -0.05\ \mathrm{K}^{-1}$ (optimistic)		7.8×10^{-12}
$\gamma = 1\times10^{12}$ rad/s (low disorder)		9.4×10^{-12}
$\gamma = 5\times10^{12}$ rad/s (nominal)		1.3×10^{-11}
$\gamma = 1\times10^{13}$ rad/s (high disorder)		2.1×10^{-11}

Monte Carlo simulation uses $N_{\mathrm{MC}} = 20000$ realizations. The brightness temperature:

$$T_b = T_s \mathrm{e}^{-\kappa X} + T_{bg}\left(1-\mathrm{e}^{-\kappa X}\right), \tag{12}$$

with $T_s = 290$ K and $T_{bg} = 2.7$ K. Here κ [m⁻¹] is the effective volume absorption coefficient of the atmospheric column at 1 THz (a combined opacity from H₂O vapor and trace gases), and X [m] is the integrated column thickness (path length times species mixing ratio). For the baseline simulation, $\kappa = 0.1\ \mathrm{m}^{-1}$ and

$X = 2.0$ m are adopted, representative of a limb-sounding geometry through a 10-km moist-troposphere layer at mid-latitudes [13] [35]. The retrieved state vector is the single scalar $\hat{X}$; the forward model is Equation (12) with κ known; and the measurement noise in each Monte Carlo trial is drawn from $\mathcal{N}\left(0, \sigma_{T_b}^2\right)$, where $\sigma_{T_b} = \mathrm{NEP}_{\mathrm{total}} \big/ \left(\partial P_{\mathrm{inc}} / \partial T_b\right)^{-1}$ with $t_{\mathrm{int}} = 1$ s integration and $\Delta\nu = 5$ GHz bandwidth. The inversion is performed by analytically solving Equation (12) for X given the noisy T_b measurement. This radiative transfer formulation is standard in atmospheric remote sensing [35].

5. Results

5.1. NEP Sensitivity Map

Figure 3 shows the total NEP as a function of E_F and n at 1 THz. The lowest NEP ($6.4 \times 10^{-12}\ \mathrm{W}/\sqrt{\mathrm{Hz}}$) occurs near $E_F \approx 0.17$ eV and $n \approx 1.5$. Higher Fermi levels enhance the intraband conductivity, boosting responsivity and reducing Johnson and amplifier noise. For practical regimes with moderate $n \approx 3$, an NEP of $1.3 \times 10^{-11}\ \mathrm{W}/\sqrt{\mathrm{Hz}}$ is achieved at $E_F \approx 0.4$ eV.

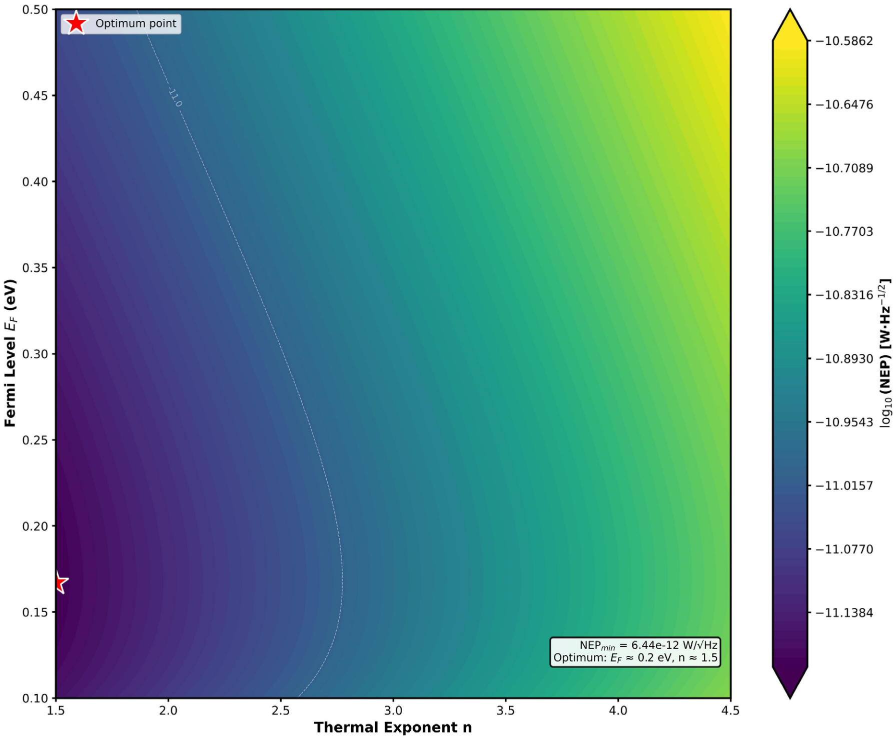

Figure 3. Logarithm of total NEP ($\mathrm{W}/\sqrt{\mathrm{Hz}}$) vs. graphene Fermi level E_F and thermal exponent n at $f = 1$ THz, $T_{\mathrm{bath}} = 300$ K.

5.2. Frequency-Dependent Absorption and Responsivity

Figure 4 shows the absorption for five Fermi levels. The peak near 1 THz is due to the quarter-wave design, with tunability via gating. Panel (b) displays the effective responsivity, confirming that spectral response can be tuned by gating.

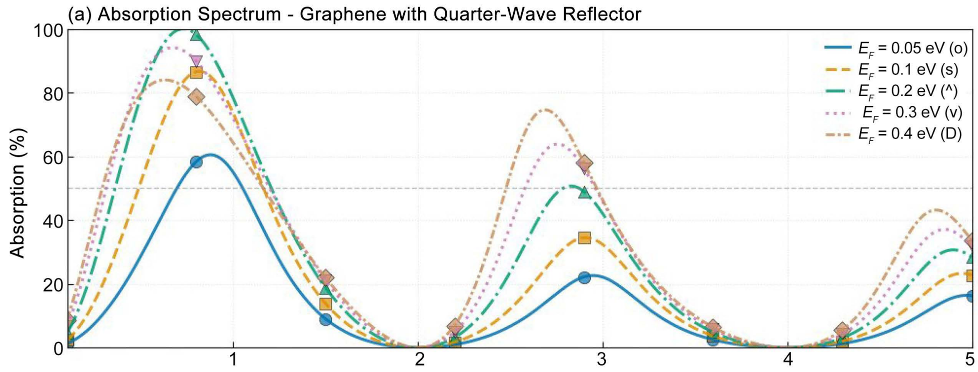
(a) Absorption Spectrum - Graphene with Quarter-Wave Reflector

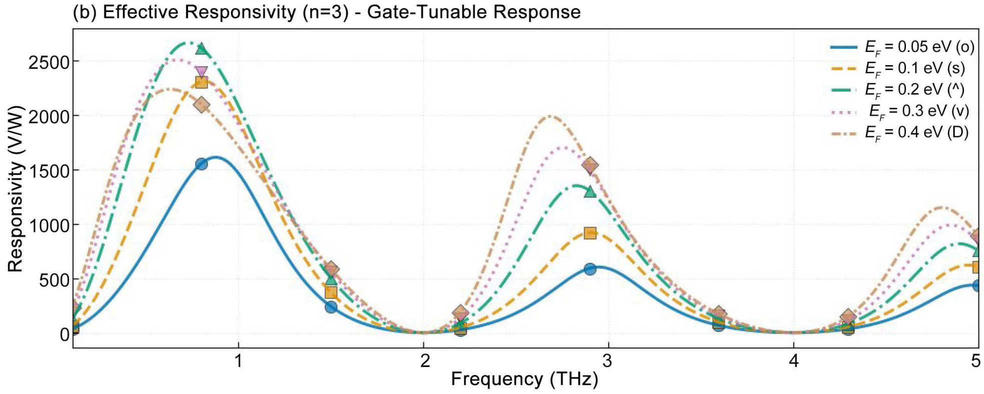
(b) Effective Responsivity (n=3) - Gate-Tunable Response

Figure 4. (a) Absorption of graphene with quarter-wave reflector for $E_F = 0.05, 0.1, 0.2, 0.3, 0.4$ eV. (b) Effective responsivity for $n = 3$.

5.3. Benchmarking against State-of-the-Art

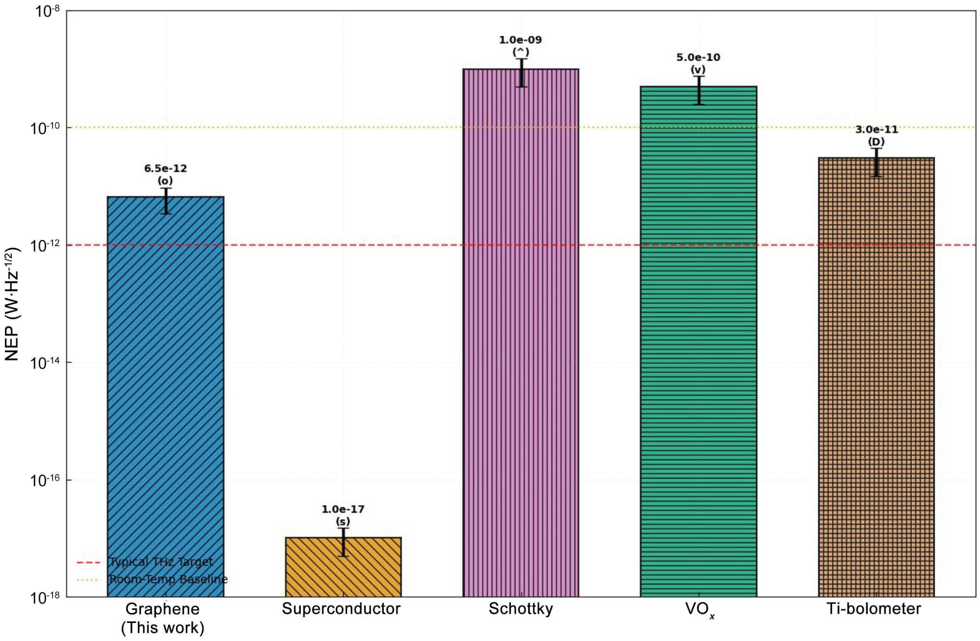

Figure 5. NEP comparison with state-of-the-art THz detectors (error bars indicate typical ranges from literature).

Figure 5 compares our modeled detector with representative THz detector technologies, including error bars for robustness based on literature ranges. The graphene microbolometer outperforms uncooled Schottky diodes and VO_x bolometers in the modeled regime [7] [8].

5.4. Trade-Off between Speed and Sensitivity

Figure 6 shows the NEP components as a function of thermal time constant $\tau = C/G$. The optimum point ($\tau \approx 3.2$ ms, $\text{NEP} \approx 2.9\times10^{-13}\ \text{W}/\sqrt{\text{Hz}}$) is indicated. The secondary top axis shows the corresponding electrical bandwidth $f_{\text{3dB}} = 1/(2\pi\tau)$.

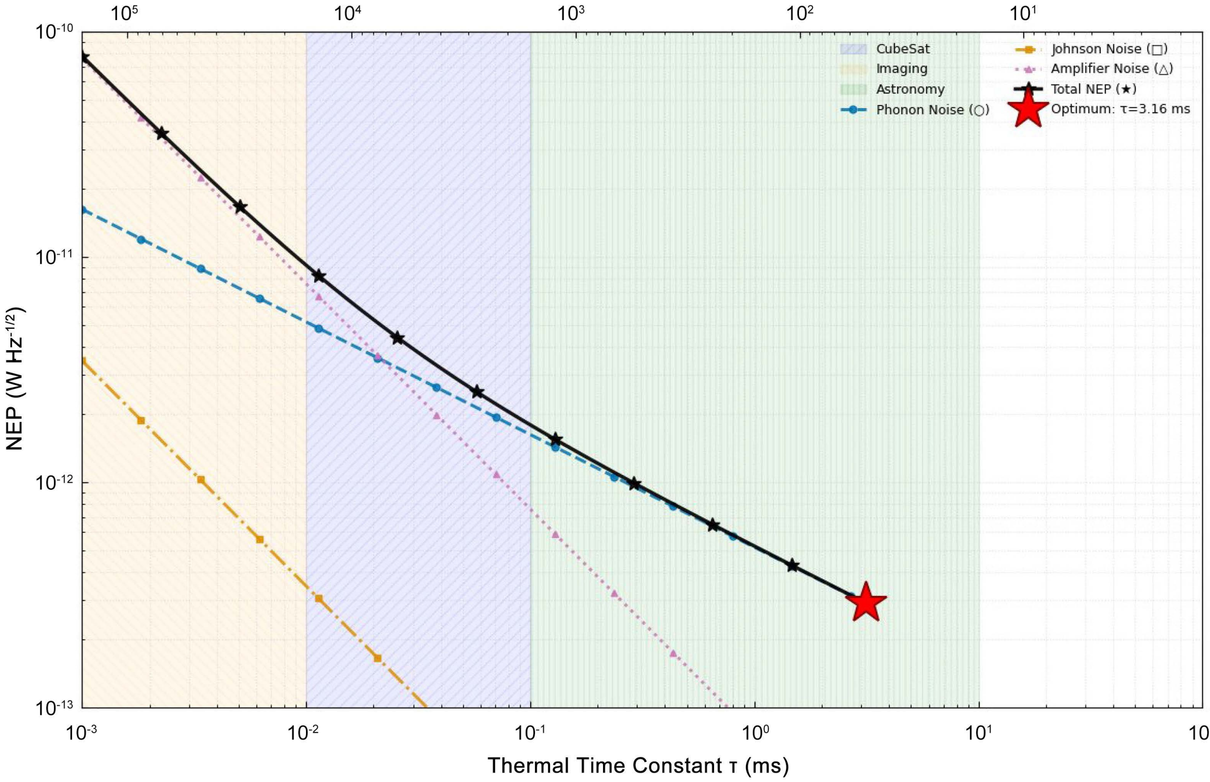

Figure 6. NEP components vs. thermal time constant τ. Shaded regions indicate typical application domains. The secondary axis shows the equivalent 3 dB bandwidth.

5.5. Influence of Bath Temperature

Figure 7 shows NEP versus bath temperature for five n values. Moderate cooling (to 200 K) reduces NEP by a factor of 2 - 3, which can be achieved by passive radiators or small Stirling coolers on CubeSats [5].

5.6. Retrieval Uncertainty

Monte Carlo simulation results (**Figure 8**) show the distribution of retrieved column thickness. The standard deviation is 0.01 m (0.5% relative uncertainty), meeting typical science requirements for limb sounding [13] [35].

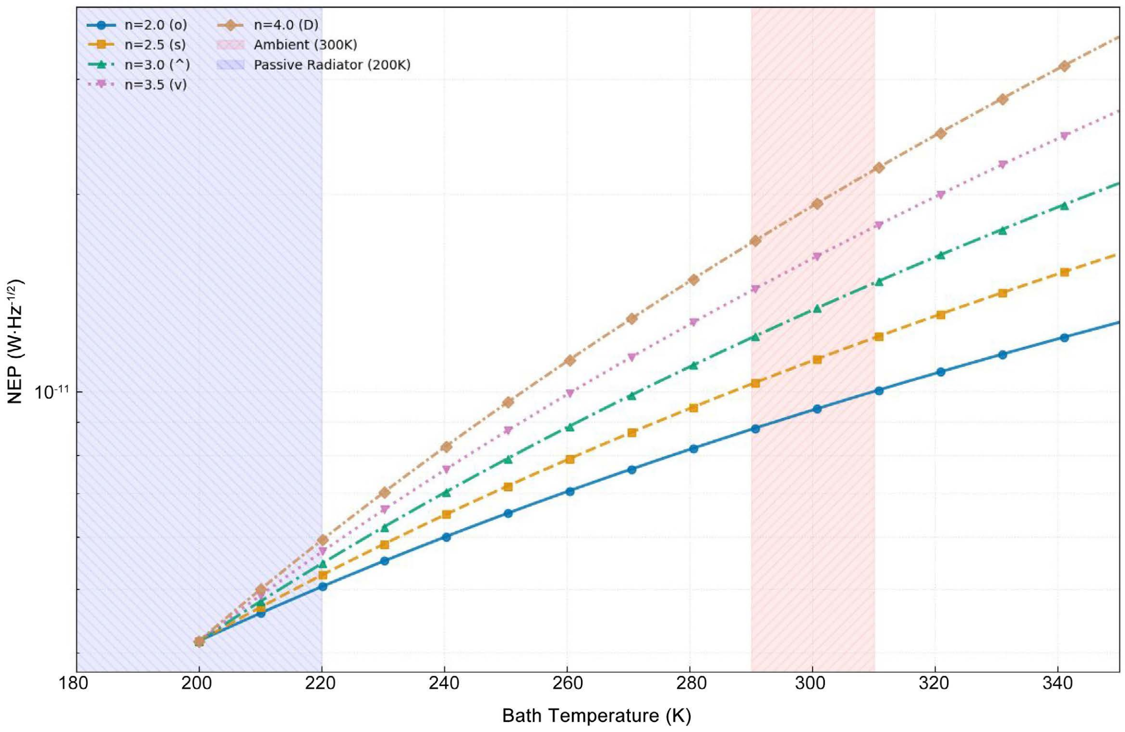

Figure 7. NEP dependence on bath temperature for $n = 2.0, 2.5, 3.0, 3.5, 4.0$.

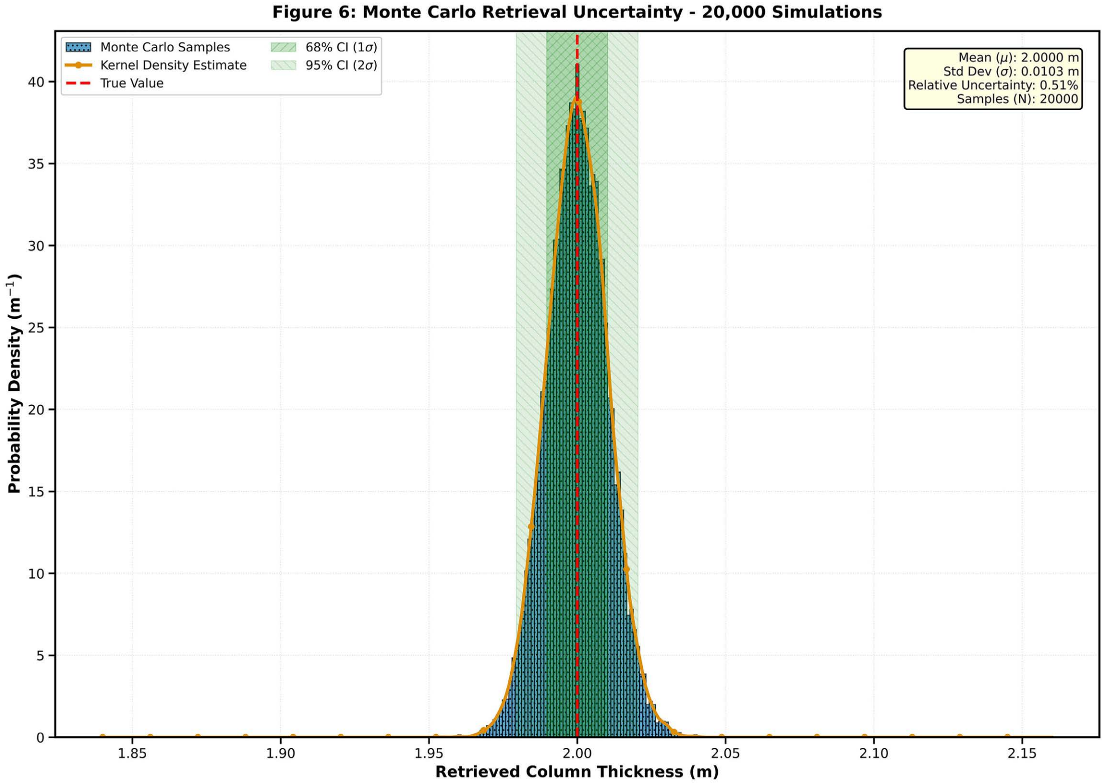

Figure 8. Histogram of retrieved column thickness from 20,000 Monte Carlo trials. True value is 2.0 m. The red curve is a kernel density estimate; shaded regions indicate 68% and 95% confidence intervals. Statistics: $\mu = 2.000$ m, $\sigma = 0.01$ m, relative uncertainty = 0.5%.

6. Discussion

6.1. Achievability of Design Parameters: TCR

A significant technical challenge is achieving the assumed TCR of $\alpha = -0.03\ \text{K}^{-1}$. To achieve this, careful engineering of the following parameters is required [24] [36]:

1) **Contact material**: Nickel and Palladium exhibit lower Schottky barrier heights.

2) **Doping and defects**: Minimize charge traps using dielectric encapsulation.

3) **Gate geometry**: Maximize gate capacitance for enhanced field-effect mobility.

6.2. Limitations of the Thermal Conductance Model

The power-law model assumes a single dominant transport mechanism across 200 - 300 K. In reality, the exponent n may transition between different regimes. Real devices should be characterized experimentally to measure $G(T)$ over the entire operational temperature range [25].

6.3. Absorption Design: Beyond Fixed Spacers

For broadband coverage (0.1 - 1.5 THz), several approaches exist [9] [11]:

1) Variable spacer thickness via multi-layer stacks

2) Antenna-coupled designs with enhanced bandwidth

3) Gradient-index structures for broadband impedance matching

The leakage current through a 10-nm HfO_2 dielectric is typically below 1 nA/μm^2 at 8.5 V, yielding $\lesssim 1$ μW for a 1-mm^2 pixel—negligible in the power budget. Gate voltage stability of ±10 mV (achievable with standard DAC designs) corresponds to a Fermi-level uncertainty of ±0.05 meV, which shifts the absorption peak by <0.05 GHz and has a negligible effect on the reported NEP.

Contact resistance and spatial non-uniformity of E_F are additional concerns. Contact resistance R_c adds in series with R_{det} and increases the Johnson noise contribution; for R_c ~100 Ω μm (Ni or Pd contacts on graphene [36]) on a 1-mm-wide channel, $R_c < 0.1\ \Omega$, contributing < 0.02% to the noise budget. Spatial non-uniformity of E_F across the pixel (typically ±5% in high-quality CVD graphene on flat gates) translates to a ±1% variation in absorption and responsivity, which must be calibrated in flight.

6.4. System-Level Implications for CubeSat

Integration with low-noise CMOS readout electronics is essential. Modern transimpedance amplifiers achieve gain of 10^7 - 10^8 V/A with input-referred noise of 10 - 30 $\text{nV}/\sqrt{\text{Hz}}$ and power consumption < 10 mW. Thermal stabilization to ±5 K is achievable via passive radiators or small Stirling coolers. Total instrument mass of 300 - 500 g is realistic [5].

6.5. Path Forward: Experimental Validation

The next phase requires [9] [10]:

1) Prototype fabrication with well-characterized TCR.
2) NEP characterization as a function of bias and Fermi level.
3) Multi-spectral tuning demonstration.
4) Thermal vacuum testing.
5) Flight model development and space qualification.

7. Conclusions

We have developed a comprehensive, physics-based model of a graphene-enhanced THz microbolometer that integrates thermal response, electromagnetic absorption via admittance modeling, and fundamental noise sources. An explicit end-to-end measurement chain links scene spectral radiance through optical etendue and absorption efficiency to output voltage, providing a traceable path from NEP to retrieval noise in Monte Carlo simulations. The model quantifies trade-offs and identifies an optimal design space ($E_F \approx 0.4$ eV, $n \approx 3$) achieving an NEP of $1.3\times10^{-11}\ \mathrm{W}/\sqrt{\mathrm{Hz}}$ at 1 THz, with a minimum of $6.4\times10^{-12}\ \mathrm{W}/\sqrt{\mathrm{Hz}}$ in extreme regimes. A one-at-a-time sensitivity analysis shows that NEP degrades by 3× if TCR drops from −0.03 to −0.01 K^{-1}, and by ~60% if the graphene scattering rate doubles, motivating tight process control. A gate feasibility analysis shows that the target $E_F \approx 0.4$ eV is reachable below 10 V using a high-k top gate, compatible with space-qualified low-voltage electronics. Monte Carlo retrievals show column thickness uncertainties around 0.5%, meeting science requirements. The framework provides a rigorous baseline for developing compact THz instruments for CubeSat-based Earth observation.

Conflicts of Interest

The authors declare no conflicts of interest regarding the publication of this paper.

References

[1] Waters, J.W., Froidevaux, L., Harwood, R.S., Jarnot, R.F., *et al.* (2006) The Earth Observing System Microwave Limb Sounder (EOS MLS) on the Aura Satellite. *IEEE Transactions on Geoscience and Remote Sensing*, **44**, 1075-1092.

[2] Siegel, P.H. (2002) Terahertz technology. *IEEE Transactions on Microwave Theory and Techniques*, **50**, 910-928. https://doi.org/10.1109/22.989974

[3] Roelfsema, P.R., Helmich, F.P., Teyssier, D., *et al.* (2012) In-Orbit Performance of Herschel-HIFI. *Astronomy & Astrophysics*, **537**, A17.

[4] Griffin, M.J., Abergel, A., Abreu, A., *et al.* (2010) The Herschel-SPIRE Instrument and Its In-Flight Performance. *Astronomy & Astrophysics*, **518**, L3.

[5] Woellert, K., Ehrenfreund, P., Ricco, A.J. and Hertzfeld, H. (2011) Cubesats: Cost-Effective Science and Technology Platforms for Emerging and Developing Nations. *Advances in Space Research*, **47**, 663-684. https://doi.org/10.1016/j.asr.2010.10.009

[6] Selva, D. and Krejci, D. (2012) A Survey and Assessment of the Capabilities of Cubesats for Earth Observation. *Acta Astronautica*, **74**, 50-68. https://doi.org/10.1016/j.actaastro.2011.12.014

[7] Rogalski, A. (2010) Infrared and Terahertz Detectors. CRC Press.

[8] Sizov, F. and Rogalski, A. (2010) THz Detectors. *Progress in Quantum Electronics*, **34**, 278-347. https://doi.org/10.1016/j.pquantelec.2010.06.002

[9] Ju, L., Geng, B., Horng, J., Girit, C., Martin, M., Hao, Z., *et al.* (2011) Graphene Plasmonics for Tunable Terahertz Metamaterials. *Nature Nanotechnology*, **6**, 630-634. https://doi.org/10.1038/nnano.2011.146

[10] Vicarelli, L., Vitiello, M.S., Coquillat, D., Lombardo, A., Ferrari, A.C., Knap, W., *et al.* (2012) Graphene Field-Effect Transistors as Room-Temperature Terahertz Detectors. *Nature Materials*, **11**, 865-871. https://doi.org/10.1038/nmat3417

[11] Sensale-Rodriguez, B., Yan, R., Rafique, S., *et al.* (2013) Extraordinary Control of Terahertz Beam Reflectance in Graphene Electro-Absorption Modulators. *Nano Letters*, **13**, 1904-1909.

[12] Tamagnone, M., *et al.* (2014) Ultra-Broadband Terahertz Absorption in Graphene Microribbons. *Applied Physics Letters*, **105**, Article 061108.

[13] Livesey, N.J., Van Snyder, W., Read, W.G. and Wagner, P.A. (2006) Retrieval Algorithms for the EOS Microwave Limb Sounder (MLS). *IEEE Transactions on Geoscience and Remote Sensing*, **44**, 1144-1155. https://doi.org/10.1109/tgrs.2006.872327

[14] Pilbratt, G.L., Riedinger, J.R., Passvogel, T., Crone, G., Doyle, D., Gageur, U., *et al.* (2010) Herschel Space Observatory. An ESA Facility for Far-Infrared and Submillimetre Astronomy. *Astronomy & Astrophysics*, **518**, L1.

[15] Blackwell, W.J., *et al.* (2018) MicroMAS-2: A 3U CubeSat for TROPICS Pathfinder. 2018 *IEEE Aerospace Conference*, *Montana*, 3-10 March 2018, 1-12.

[16] Lewis, R.A. (2014) A Review of Terahertz Sources. *Journal of Physics D*: *Applied Physics*, **47**, Article 374001. https://doi.org/10.1088/0022-3727/47/37/374001

[17] Popescu, C., *et al.* (2019) Terahertz Microbolometers Based on Micromachined Structures. *Sensors*, **19**, Article 556.

[18] Padilla, W.J., Taylor, A.J., Highstrete, C., Lee, M. and Averitt, R.D. (2006) Dynamical Electric and Magnetic Metamaterial Response at Terahertz Frequencies. *Physical Review Letters*, **96**, Article 107401. https://doi.org/10.1103/physrevlett.96.107401

[19] Falkovsky, L.A. (2008) Optical Properties of Graphene. *Journal of Physics*: *Conference Series*, **129**, Article 012004. https://doi.org/10.1088/1742-6596/129/1/012004

[20] Low, T. and Avouris, P. (2014) Graphene Plasmonics for Terahertz to Mid-Infrared Applications. *ACS Nano*, **8**, 1086-1101. https://doi.org/10.1021/nn406627u

[21] Koppens, F.H.L., Chang, D.E. and García de Abajo, F.J. (2011) Graphene Plasmonics: A Platform for Strong Light-Matter Interactions. *Nano Letters*, **11**, 3370-3377. https://doi.org/10.1021/nl201771h

[22] Mak, K.F., Sfeir, M.Y., Wu, Y., Lui, C.H., Misewich, J.A. and Heinz, T.F. (2008) Measurement of the Optical Conductivity of Graphene. *Physical Review Letters*, **101**, Article 196405. https://doi.org/10.1103/physrevlett.101.196405

[23] Andryieuski, A. and Lavrinenko, A.V. (2013) Graphene Metamaterials Based Tunable Terahertz Absorber: Effective Surface Conductivity Approach. *Optics Express*, **21**, Article 9144. https://doi.org/10.1364/oe.21.009144

[24] Balandin, A.A., Ghosh, S., Bao, W., Calizo, I., Teweldebrhan, D., Miao, F., *et al.* (2008) Superior Thermal Conductivity of Single-Layer Graphene. *Nano Letters*, **8**, 902-907. https://doi.org/10.1021/nl0731872

[25] Pop, E. (2010) Energy Dissipation and Transport in Nanoscale Devices. *Nano Research*, **3**, 147-169. https://doi.org/10.1007/s12274-010-1019-z

[26] Smith, D.R., Pendry, J.B. and Wiltshire, M.C.K. (2004) Metamaterials and Negative Refractive Index. *Science*, **305**, 788-792. https://doi.org/10.1126/science.1096796

[27] Schurig, D., Mock, J.J., Justice, B.J., Cummer, S.A., Pendry, J.B., Starr, A.F., *et al.* (2006) Metamaterial Electromagnetic Cloak at Microwave Frequencies. *Science*, **314**, 977-980. https://doi.org/10.1126/science.1133628

[28] Vakil, A. and Engheta, N. (2011) Transformation Optics Using Graphene. *Science*, **332**, 1291-1294. https://doi.org/10.1126/science.1202691

[29] García de Abajo, F.J. (2014) Graphene Plasmonics: Challenges and Opportunities. *ACS Photonics*, **1**, 135-152. https://doi.org/10.1021/ph400147y

[30] Richards, P.L. (1994) Bolometers for Infrared and Millimeter Waves. *Journal of Applied Physics*, **76**, 1-24. https://doi.org/10.1063/1.357128

[31] Mather, J.C. (1982) Bolometer Noise: Nonequilibrium Theory. *Applied Optics*, **21**, Article 1125. https://doi.org/10.1364/ao.21.001125

[32] Nyquist, H. (1928) Thermal Agitation of Electric Charge in Conductors. *Physical Review*, **32**, 110-113. https://doi.org/10.1103/physrev.32.110

[33] Johnson, J.B. (1928) Thermal Agitation of Electricity in Conductors. *Physical Review*, **32**, 97-109. https://doi.org/10.1103/physrev.32.97

[34] Nair, R.R., Blake, P., Grigorenko, A.N., Novoselov, K.S., Booth, T.J., Stauber, T., *et al.* (2008) Fine Structure Constant Defines Visual Transparency of Graphene. *Science*, **320**, 1308-1308. https://doi.org/10.1126/science.1156965

[35] Rodgers, C.D. (2000). Inverse Methods for Atmospheric Sounding. World Scientific. https://doi.org/10.1142/3171

[36] Xia, F., Perebeinos, V., Lin, Y., Wu, Y. and Avouris, P. (2011) The Origins and Limits of Metal-Graphene Junction Resistance. *Nature Nanotechnology*, **6**, 179-184. https://doi.org/10.1038/nnano.2011.6